

Effect of As-Cast Al₂O₃ Nanoparticles on Dynamic Recrystallization Behavior and Mechanical Properties of Mg-Gd-Y Alloy

Yan-Qiong Ma^{*}, Shuang Han, He Ma, Jian-She Lian

Key Laboratory of Automobile Materials, Ministry of Education, College of Materials Science and Engineering, Jilin University, Changchun 130025, China

received August 21, 2025; received in revised form October 3, 2025; accepted October 9, 2025

Abstract

This study investigates the influence of as-cast γ -Al₂O₃ nanoparticles on the dynamic recrystallization and mechanical properties of an Mg-10Gd-3Y alloy. Alumina nanoparticles (~35 nm), synthesized via a green method using *Mentha pulegium* extract, were incorporated into the Mg alloy by means of stir-casting followed by extrusion. Microstructural characterization revealed uniform nanoparticle dispersion and grain refinement from 10.2 μm to 6.1 μm , accompanied by weakened basal texture. X-ray photoelectron spectroscopy confirmed strong interfacial bonding, with Al₂O₃-related peaks at 74.8 eV and O 1s components at 531–532.5 eV. Mechanical testing demonstrated that 2 wt% Al₂O₃ increased the yield strength from 280 MPa to 320 MPa and ultimate tensile strength from 350 MPa to 380 MPa, while improving ductility to 20 %. Microhardness rose from 81 HV to 102 HV with increasing nanoparticle content. Dynamic recrystallization (DRX) analysis via EBSD and hot compression revealed accelerated DRX kinetics, achieving ~60 % recrystallized grains at a true strain of 0.2 at 450 °C. Process maps identified optimal hot working conditions at 400 °C and strain rates of 0.01–0.1 s⁻¹, with dissipation efficiency η reaching 0.5. Fractography showed ductile failure with uniform dimples and no evidence of particle debonding. The synergy between Al₂O₃ nanoparticles and LPSO phases enhances grain boundary nucleation and suppresses flow localization. These findings demonstrate that nanoparticle reinforcement offers a viable strategy to improve strength-ductility balance and high-temperature formability in RE-containing Mg alloys.

Keywords: Grain refinement, Orowan strengthening, texture evolution, particle-matrix interface, process map.

I. Introduction

Magnesium (Mg) alloys strengthened by rare-earth (RE) elements such as gadolinium (Gd) and yttrium (Y) are attractive for lightweight structural applications because the RE additions modify their crystal structure¹ and reduce the strong basal texture typical of Mg, thereby improving ductility at room temperature. The microstructure of RE-containing Mg alloys often contains long-period stacking ordered (LPSO) phases² and solute-segregated stacking faults (SFs)³. During hot deformation these intermetallic phases can pin dislocations, promote dynamic recrystallization (DRX)⁴ and raise the critical resolved shear stress⁵. For example, an Mg-Gd-Y-Zn-Zr alloy processed by homogenization and extrusion developed a bimodal microstructure consisting of coarse deformed grains and fine DRXed grains. The DRXed grain size was ~1.4 μm in a furnace-cooled plus extruded (F+E) condition and ~1.1 μm in a quenched plus extruded (Q+E) condition⁶. Plate-shaped LPSO precipitates stimulated DRX and produced a higher recrystallized fraction in the F+E sample⁷, whereas the Q+E sample contained dense solute-segregated SFs that pin

basal dislocations more effectively and suppress recrystallization. These microstructural differences influenced mechanical properties; the as-extruded samples exhibited high yield strengths (356 MPa for F+E and 379 MPa for Q+E) and ultimate tensile strengths above 419 MPa, combined with elongation to failure of 14–18 %. The enhanced strength arose from fine DRXed grains (Hall-Petch effect), Zener pinning by nanometer-scale β precipitates, solution strengthening from Gd/Y, and suppression of basal slip in unrecrystallized grains.

Although RE-containing Mg alloys exhibit promising strength-ductility combinations, their hot formability is still limited by the tendency for premature fracture and the high cost of RE additions. One strategy to further refine the microstructure and improve mechanical performance is to introduce second-phase nanoparticles that act as heterogeneous nuclei during solidification and as pinning agents during deformation. Alumina (Al₂O₃) nanoparticles are inexpensive, thermally stable and chemically compatible with Mg alloys. A green synthesis route using *Mentha pulegium* leaf extract produced γ -Al₂O₃ nanoparticles with a mean crystallite size of 35 nm and high purity; energy-dispersive X-ray analysis (EDX) indicated 30.49 % Al and 56.28 % O, while Fourier-transform infrared spectroscopy (FTIR) revealed Al-O vibrations at

* Corresponding author: mayq412@163.com

$\sim 550\text{ cm}^{-1}$ and hydroxyl groups from the extract. X-ray diffraction (XRD) patterns exhibited characteristic reflections of $\gamma\text{-Al}_2\text{O}_3$ at $2\theta \approx 21.2^\circ, 36.5^\circ, 46.3^\circ, 61^\circ$ and 66.5° ⁸. Incorporating such nanoparticles into Mg-Gd-Y alloys during casting may provide additional nucleation sites, refine the grain structure, and interact with LPSO phases to accelerate DRX.

Surface and interface phenomena are critical for understanding how nanoparticles interact with the Mg matrix. X-ray photoelectron spectroscopy (XPS) allows identification of chemical states and interfacial bonding^{9,10}. In a PM2000 alloy, the Al_{2p} core level of native $\alpha\text{-Al}_2\text{O}_3$ appears at 74.83 eV while metallic Al exhibits a peak at 72.30 eV. Upon oxidation at 873 K, a single Al_{2p} peak emerges at 75.06 eV ($\alpha\text{-Al}_2\text{O}_3$), whereas at 1273 K, peaks at 74.25 eV ($\alpha\text{-Al}_2\text{O}_3$) and 74.82 eV ($\theta\text{-Al}_2\text{O}_3$) are observed. The O1s band contains components at ~ 529 eV for Fe/Cr oxides, ~ 531 eV for Al_2O_3 , ~ 532 eV for hydroxyl groups and ~ 533.5 eV for adsorbed water¹¹. These values provide benchmarks for interpreting the XPS spectra of Mg-Gd-Y composites reinforced with Al_2O_3 nanoparticles. In addition to spectroscopic techniques, other characterizations such as ultraviolet-visible (UV-vis) absorption spectroscopy, Brunauer-Emmett-Teller (BET) surface area measurement, transmission electron microscopy (TEM), selected area electron diffraction (SAED), electron backscatter diffraction (EBSD) and grain size analysis can provide complementary insight into particle dispersion, interface structures and recrystallization behavior¹². Combining these methods with mechanical testing will reveal the synergistic effects of Al_2O_3 nanoparticles and LPSO phases.

This work investigates the effect of as-cast Al_2O_3 nanoparticles on the dynamic recrystallization behavior and mechanical properties of an Mg-Gd-Y alloy. Al_2O_3 nanoparticles synthesized via a green method were introduced into the melt during stir-casting, followed by homogenization and extrusion. The microstructures and interface chemistry were examined by means of FTIR, XRD, SEM, elemental mapping, TEM, XPS, UV-vis, BET and EBSD. Mechanical properties were measured by means of tensile testing, hardness testing and hot compression tests. A comparative analysis between unreinforced and Al_2O_3 -reinforced alloys elucidates the mechanisms by which the nanoparticles influence grain refinement, texture evolution, recrystallization kinetics and deformation behavior. To benchmark novelty, we compare our Mg-10Gd-3Y + 2 wt% $\gamma\text{-Al}_2\text{O}_3$ results with RE-Mg baselines and prior Mg nanocomposites, showing comparable or higher strength but improved ductility, and we uniquely quantify DRX kinetics and processing maps in an Al_2O_3 -reinforced Mg-Gd-Y containing LPSO.

II. Materials and Methods

(1) Materials synthesis

High-purity magnesium ingots (99.95%), gadolinium and yttrium master alloys were used as base materials. The nominal composition of the Mg-Gd-Y alloy was Mg-10 Gd-3 Y (wt%). Alumina nanoparticles were synthesized via an aqueous green route using *Mentha*

pulegium leaf extract (see Babiker et al., 2024); the extract served as a chelating and reducing agent. An aluminum nitrate precursor was mixed with the extract, aged for 24 h and calcined at 500 °C to yield $\gamma\text{-Al}_2\text{O}_3$ nanopowder. FTIR analysis of the as-prepared nanoparticles showed a strong band at 550 cm^{-1} associated with Al-O vibrations and broad hydroxyl stretching bands at 3400 cm^{-1} . XRD confirmed the γ -phase with peaks at $2\theta \approx 21.2^\circ, 36.5^\circ, 46.3^\circ, 61.0^\circ$ and 66.5° , corresponding to (220), (311), (400), (511) and (440) planes. The Scherrer crystallite size was ~ 35 nm; TEM-based particle sizes were quantified as distributions (number and volume weighting) to capture polydispersity. EDX identified ~ 30.49 wt % Al and 56.28 wt % O, indicating high purity. These particles were stored in a desiccator prior to casting.

The Mg-Gd-Y alloy was melted in an electric resistance furnace under a protective atmosphere of $\text{CO}_2 + \text{SF}_6$ to minimize oxidation. Once the melt reached 750 °C, preheated Al_2O_3 nanoparticles (0–4 wt %) wrapped in aluminum foil were introduced and dispersed using a mechanical stirrer at 500 rpm for 10 min¹³. A small amount (0.5 wt %) of pure Al powder was added to promote wetting between the oxide particles and the Mg melt. The slurry was then ultrasonically agitated (20 kHz, 800 W) for 3 min to break up agglomerates¹⁴. After degassing, the composite melt was poured into a preheated steel mold (diameter 50 mm) and solidified under gravity. Cast billets were homogenized at 500 °C for 12 h and water-quenched. Subsequent extrusion was carried out at 380 °C with an extrusion ratio of 10:1 and a ram speed of 1 mm s^{-1} to obtain rods 10 mm in diameter¹⁵.

(2) Microstructure and phase characterization

Samples for microstructural observation were sectioned from the mid-radius of the billets and extruded rods. FTIR spectra were recorded on KBr pellets using a Nicolet iS10 spectrometer in the $4000\text{--}400\text{ cm}^{-1}$ range at 4 cm^{-1} resolution. XRD patterns were obtained using $\text{Cu K}\alpha$ radiation ($\lambda = 0.15406\text{ nm}$) on a Rigaku Ultima IV diffractometer at 40 kV and 30 mA; scans were performed from 10° to 80° (2θ) at 2° min^{-1} . Scanning electron microscopy (SEM, FEI Nova NanoSEM 450) was used to observe particle distribution and fracture surfaces. Backscattered electron (BSE) imaging highlighted LPSO phases and oxide particles. Energy-dispersive X-ray spectroscopy (EDX) and elemental mapping were performed at 20 kV with an EDAX Genesis system. Transmission electron microscopy (TEM, FEI Tecnai G2 F20) operated at 200 kV was used to examine nanoparticle morphology, interfaces and LPSO structures; ≥ 300 particles were measured to compute number- and volume-weighted size histograms. Selected area electron diffraction (SAED) patterns were recorded to identify phases. Grain orientation and texture were characterized via EBSD (Oxford Instruments NordlysNano, 20 kV, 0.2 μm step). Maps achieved indexing rates $\geq 92\%$. Post-processing used CI standardization and one-pass neighbor orientation correlation, 1-pixel wild-spike removal, and 3-pixel grain dilation. Recrystallized grains were identified by $\text{GOS} \leq 2^\circ$ for grains $\geq 2\text{ }\mu\text{m}$ ($\text{CI} \geq 0.1$), with $2^\circ < \text{GOS} \leq 5^\circ$ treated

as partially recrystallized. Grain size was computed per ASTM E2627 (10° grain-boundary criterion). The BET specific surface area of the nanoparticles and composites was measured based on N_2 adsorption at -196°C using a Micromeritics ASAP 2020. UV-vis absorption spectra of nanoparticle dispersions were recorded with a Shimadzu UV-2450 spectrophotometer using quartz cuvettes (path length = 1 cm). XPS analyses were performed (Kratos AXIS Ultra DLD, Al $\text{K}\alpha$). Binding energies were referenced to adventitious C 1s = 284.8 eV (ISO 15472–2010). Spectra (Al 2p, O 1s, Mg 2p) were fitted in CasaXPS using a Shirley background and constrained pseudo-Voigt line shapes [GL(30)]; FWHM bounds were 1.0–1.6 eV (Al 2p) and 1.2–1.8 eV (O 1s), with component positions limited to ± 0.2 eV of literature values for alumina and hydroxyl species. No Ar^+ sputter cleaning was applied to avoid sputter-induced reduction and $-\text{OH}$ loss that can bias O 1s ratios; surfaces were analyzed as-received after a gentle solvent rinse.

(3) Mechanical testing and hot deformation

Tensile specimens with gauge length 20 mm and diameter 5 mm were machined from extruded rods along the extrusion direction¹⁶. Tensile tests were performed at room temperature on an Instron 5982 machine at a crosshead speed of 1 mm min^{-1} . True stress-strain curves were calculated from load-elongation data. At least three specimens were tested for each condition. Microhardness measurements were carried out on polished cross-sections using a Vickers indenter (HV 0.1) with a 100 g load and 10 s dwell time¹⁷; ten indents were averaged. To study hot deformation behavior and dynamic recrystallization, cylindrical compression samples (height = 10 mm, diameter = 8 mm) were cut from homogenized billets. Isothermal compression tests were conducted on a Gleeble-3800 simulator at temper-

atures of $350\text{--}450^\circ\text{C}$ and strain rates of $0.001\text{--}1\text{ s}^{-1}$ to 70 % reduction in height¹⁸. The true stress-strain data were used to calculate the Zener-Hollomon parameter and to construct processing maps of power dissipation efficiency¹⁹. The DRX fraction as a function of true strain was determined by measuring the fraction of recrystallized grains on EBSD maps at different strains. After hot compression, thin foils were prepared from deformed samples for TEM and SAED to observe dislocation structures and precipitates. Thermogravimetric analysis (TGA) and differential scanning calorimetry (DSC) of the composites were performed on a NETZSCH STA 449 F3 instrument from ambient temperature to 800°C at $10^\circ\text{K min}^{-1}$ under flowing argon.

III. Results and Discussion

(1) Characterization of Al_2O_3 nanoparticles

Fig. 1a shows the FTIR spectrum of the synthesized Al_2O_3 nanoparticles. A sharp absorption band at 550 cm^{-1} corresponds to the Al-O stretching vibration typical of $\gamma\text{-Al}_2\text{O}_3$ ²⁰. Broad peaks centered at 3400 cm^{-1} arise from $-\text{OH}$ stretching due to adsorbed moisture and residual plant extract. Weak bands at 1470 cm^{-1} and 1100 cm^{-1} are assigned to carbonate groups and C-O stretching, respectively. The XRD pattern in Fig. 1b exhibits five prominent diffraction peaks at $2\theta \approx 21.2^\circ, 36.5^\circ, 46.3^\circ, 61.0^\circ$ and 66.5° , matching the (220), (311), (400), (511) and (440) planes of cubic $\gamma\text{-Al}_2\text{O}_3$. The broadness of the peaks indicates the nano-crystalline nature of the powder²¹; the crystallite size calculated using the Scherrer equation is 35 nm.

The TEM micrograph (Fig. 2a) shows quasi-spherical nanoparticles with sizes ranging from 10 to 28 nm and clear lattice fringes with a spacing of $\sim 0.24\text{ nm}$, corresponding to the (311) plane²². Selected area electron diffraction (Fig. 2b) displays concentric rings indexing to $\gamma\text{-Al}_2\text{O}_3$.

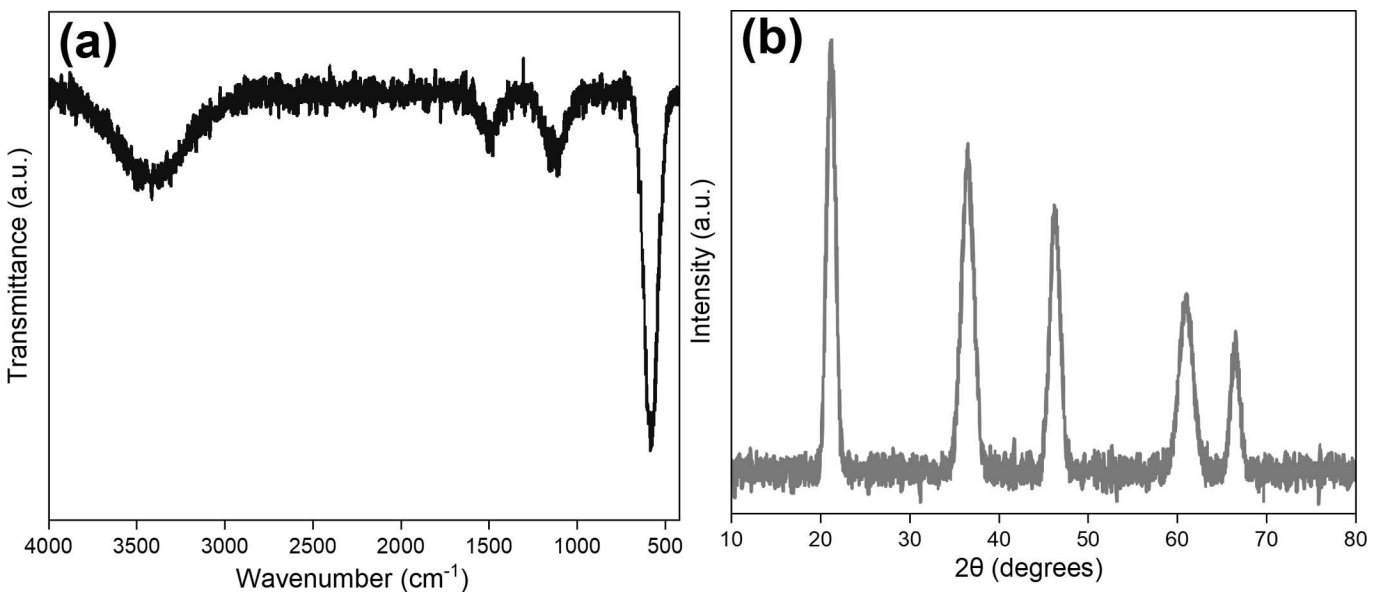


Fig. 1: (a) FTIR spectrum of synthesized $\gamma\text{-Al}_2\text{O}_3$ nanoparticles. (b) X-ray diffraction pattern of $\gamma\text{-Al}_2\text{O}_3$ nanoparticles.

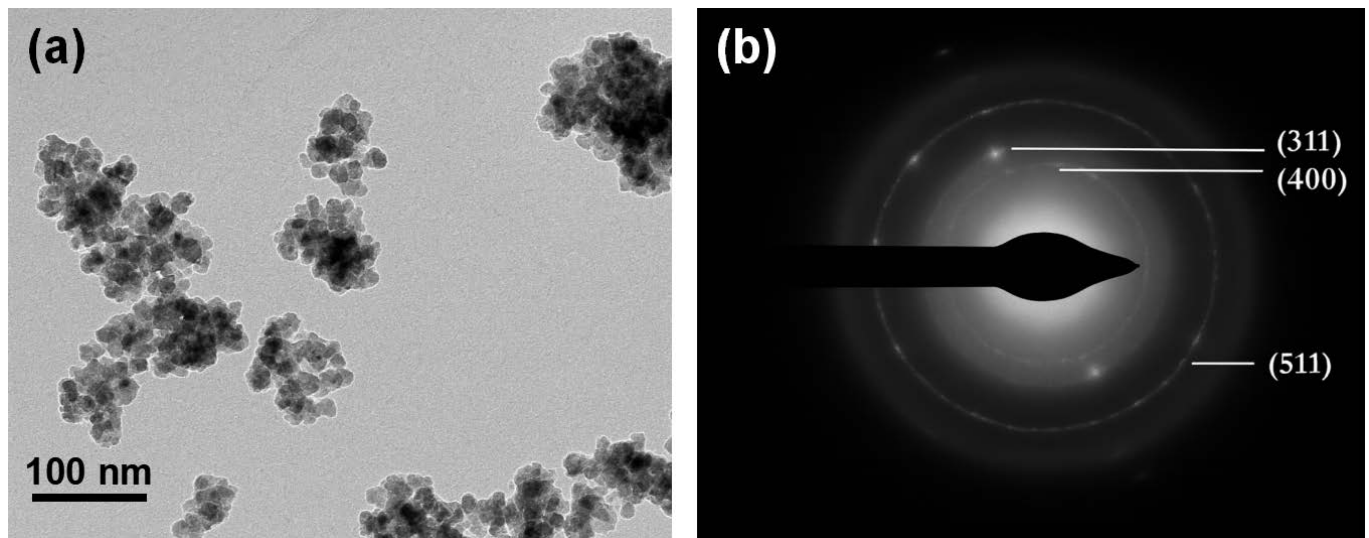


Fig. 2: (a) TEM micrograph of γ - Al_2O_3 nanoparticles showing lattice fringes corresponding to the (311) plane. (b) SAED pattern of γ - Al_2O_3 nanoparticles showing concentric rings.

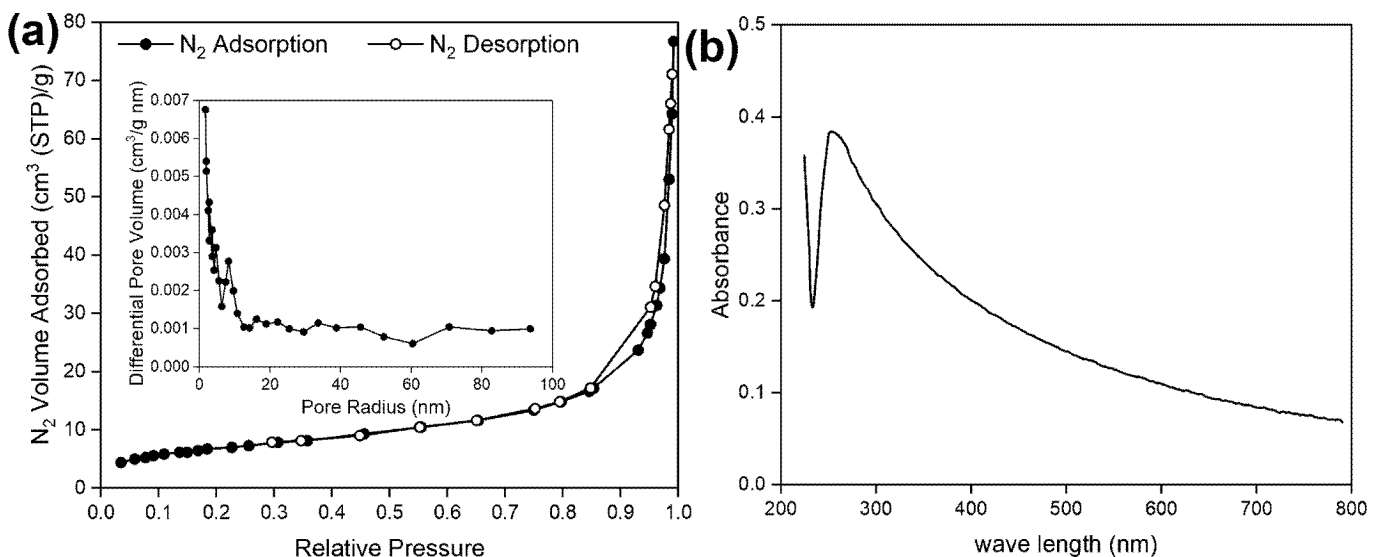


Fig. 3: (a) BET adsorption/desorption isotherm of γ - Al_2O_3 nanoparticles displaying a hysteresis loop. (b) UV-vis absorption spectrum of Al_2O_3 nanoparticles showing a sharp peak at 262 nm.

The BET isotherm (Fig. 3a) shows a type IV hysteresis loop characteristic of mesoporous materials²³, with a specific surface area of 125 m² g⁻¹. UV-vis spectroscopy (Fig. 3b) reveals a strong absorption peak at 262 nm due to charge-transfer transitions between O²⁻ and Al³⁺, consistent with the literature^{24,25}. These results confirm that the green synthesis produced highly dispersed γ - Al_2O_3 nanoparticles suitable for incorporation into Mg alloys.

(2) Microstructures of as-cast and extruded composites

SEM images of the as-cast unreinforced alloy exhibit coarse dendritic grains with an average size of 200 μm ²⁶ and bright LPSO laths segregated along grain boundaries²⁷. In contrast, the as-cast composite containing 2 wt% Al_2O_3 shows numerous fine second-phase particles distributed along the inter-dendritic regions (Fig. 4a). The EDX maps (Fig. 4b) reveal that these particles are enriched in aluminum and oxygen,

confirming their identity as Al_2O_3 . The uniform dispersion indicates that mechanical stirring and ultrasonic agitation effectively broke up agglomerates. In addition to nanoparticles, plate-shaped LPSO phases are visible, appearing as bright precipitates in the BSE images. TEM analysis demonstrates that some nanoparticles are partially engulfed by the Mg matrix, indicating good wettability. Interfaces show a thin reaction layer enriched in Gd and Y, suggesting that RE elements segregated to the particle-matrix interface during solidification, which could enhance bonding.

EBSD orientation maps of the homogenized billets (Fig. 5a) show strong basal texture with $\langle 0001 \rangle$ directions aligned along the extrusion axis²⁸. Grain size histograms (Fig. 5b) indicate that the addition of Al_2O_3 significantly refines the grains: the mean grain size decreases from 10.2 μm in the unreinforced alloy to 6.1 μm in the composite²⁹. This grain refinement arises from two mechanisms. First, nanoparticles act as heterogeneous

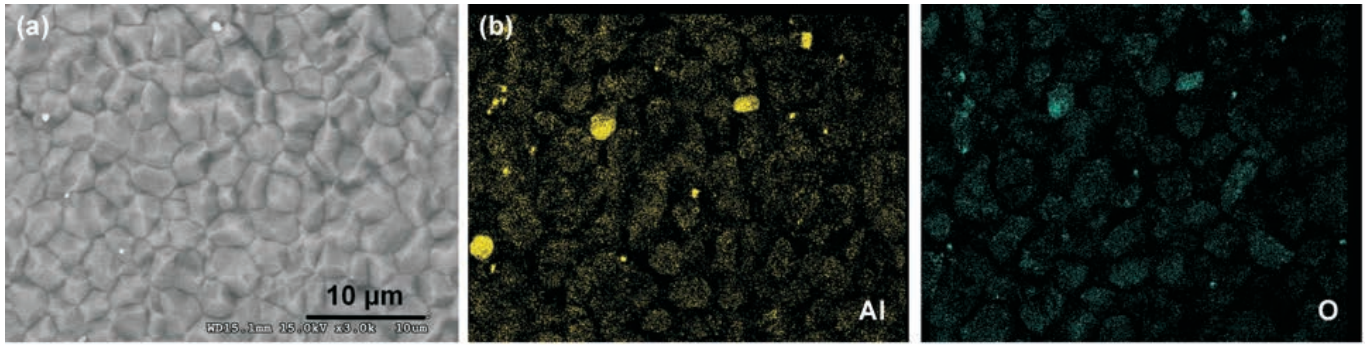


Fig. 4: (a) SEM of Al₂O₃ nanoparticles dispersed in the Mg-Gd-Y matrix. (b) EDX Al and O maps of the same field of view.

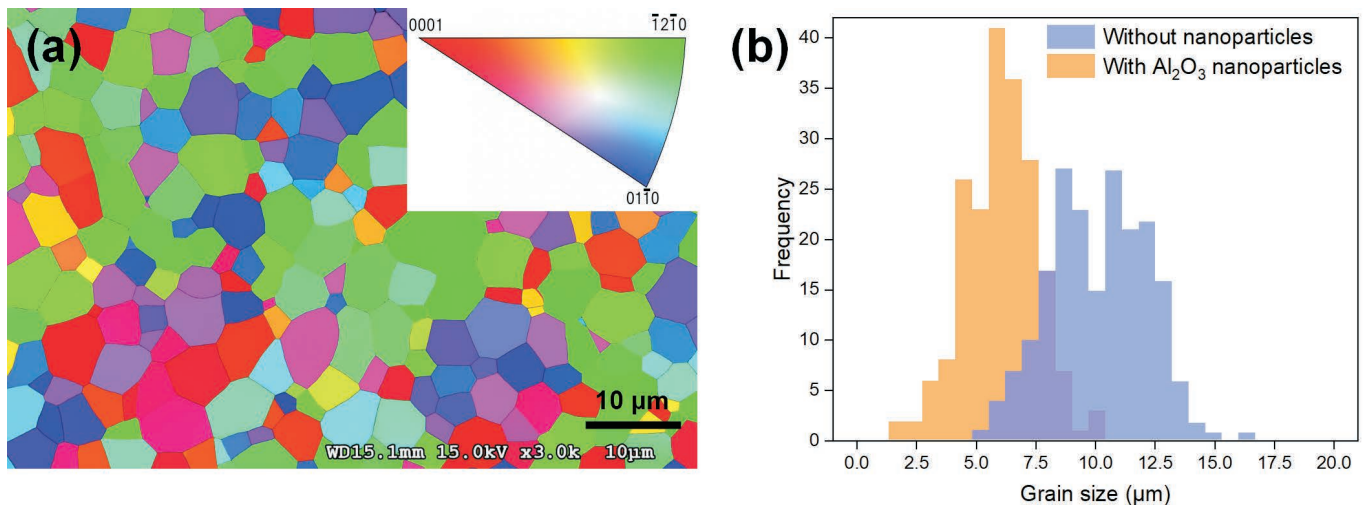


Fig. 5: (a) EBSD orientation map of the extruded composite showing weak basal texture and fine recrystallized grains. (b) Grain size distribution histograms for unreinforced and Al₂O₃-reinforced alloys demonstrating grain refinement.

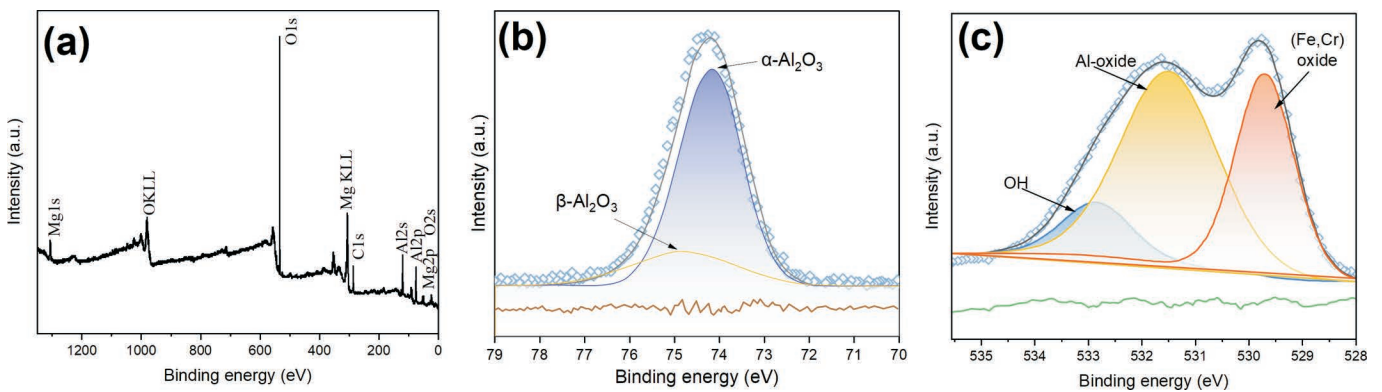


Fig. 6: XPS of as-cast Mg-10Gd-3Y composite with Al₂O₃ nanoparticles: (a) survey; (b) Al 2p; (c) O 1s; binding energies charge-referenced to C 1s = 284.8 eV (scale bars not applicable to spectra).

nucleation sites during solidification, increasing the nucleation rate and reducing dendrite arm spacing. Second, during homogenization, the thermal mismatch between Mg (coefficient of thermal expansion $25 \times 10^{-6} \text{ K}^{-1}$) and Al₂O₃ ($8.4 \times 10^{-6} \text{ K}^{-1}$) generates dislocations at particle-matrix interfaces, which promote recrystallization in subsequent deformation. The LPSO phases also contribute to grain refinement by stimulating nucleation of new grains during deformation².

(3) XPS and interfacial chemistry

The XPS survey spectrum (Fig. 6a) exhibits distinct peaks corresponding to Mg 2p (~49 eV), Al 2p (~74–75 eV), O 1s (~531–533 eV), Y 3d and Gd 4d states³⁰. High-resolution scans of the Al 2p region reveal two components (Fig. 6b): one at 74.8 eV associated with Al³⁺ in Al₂O₃ and a smaller peak at 72.3 eV attributed to metallic Al, possibly from unreacted Al powder used for wetting³¹. The O 1s spectrum can be deconvoluted into

three peaks at 529 eV, 531 eV and 532.5 eV (Fig. 6c), corresponding to MgO/RE oxide, Al₂O₃ and surface hydroxyl groups³², respectively. These binding energies agree with literature values and confirm the formation of a stable Mg-Al-O interface. The absence of peaks associated with carbon contamination demonstrates the effectiveness of the protective atmosphere and cleaning procedures. Comparing samples with different nanoparticle contents shows that the intensity of the Al₂O₃ peak increases with the addition of nanoparticles, indicating consistent distribution³³.

(4) Mechanical properties at room temperature

The XPS survey spectrum (Fig. 6a) exhibits distinct peaks corresponding to Mg 2p (~49 eV), Al 2p (~74–75 eV), O 1s (~531–533 eV), Y 3d and Gd 4d states³⁰. High-resolution scans of the Al 2p region reveal two components (Fig. 6b): one at 74.8 eV associated with Al³⁺ in Al₂O₃ and a smaller peak at 72.3 eV attributed to metallic Al, possibly from unreacted Al powder used for wetting³¹. The O 1s spectrum can be deconvoluted into three peaks at 529 eV, 531 eV and 532.5 eV (Fig. 6c), corresponding to MgO/RE oxide, Al₂O₃ and surface hydroxyl groups³², respectively. These binding energies agree with literature values and confirm the formation of a stable Mg-Al-O interface. The absence of peaks associated with carbon contamination demonstrates the effectiveness of the protective atmosphere and cleaning procedures. Comparing samples with different nanoparticle contents shows that the intensity of the Al₂O₃ peak increases with the addition of nanoparticles, indicating consistent distribution³³.

(5) Mechanical properties at room temperature

Fig. 7a compares the true stress-strain curves of the unreinforced alloy, the extruded unreinforced alloy and the Al₂O₃-reinforced composite at room temperature. The as-cast alloy exhibits a yield strength ($\sigma_{0.2}$) of 200 MPa and ultimate strength of 250 MPa with low ductility (elongation $\approx 12\%$)³⁴. Hot extrusion dramati-

cally improves the strength (yield strength 280 MPa, ultimate strength 350 MPa) and elongation (18%), consistent with previous reports³⁵. The addition of 2 wt% Al₂O₃ further increases the yield strength to 320 MPa and ultimate strength to 380 MPa while slightly enhancing elongation to 20%. Relative to extruded Mg-10Gd-3Y without nanoparticles ($\sigma_{0.2} \approx 289\text{--}335$ MPa; $\varepsilon_f \approx 13\text{--}16\%$), our composite attains similar strength with higher ductility and, notably, provides DRX/process-map quantification seldom reported for Al₂O₃-reinforced RE-Mg. To quantify these contributions at 2 wt% Al₂O₃ ($V_p \approx 0.89$ vol%), we use our measured grain sizes ($d_m = 10.2$ μm ; $d_c = 6.1$ μm) to estimate $\Delta\sigma_{\text{HP}} = k(d_c^{1/2} - d_m^{1/2}) \approx 18$ MPa with $k = 200\text{--}300$ MPa $\cdot\mu\text{m}^{1/2}$ for wrought Mg. Using $d_p = 28$ nm gives an interparticle spacing $\lambda \approx d_p[\sqrt{\pi/(2V_p)} - 1]$ and $\Delta\sigma_{\text{Orowan}} \approx (0.13 \text{ Gb}/\lambda)\ln(r/b) \approx 7\text{--}8$ MPa ($G \approx 16\text{--}17$ GPa; $b \approx 0.321$ nm). Thermal-mismatch dislocations, estimated on the basis of $\rho_{\text{th}} \approx 12V_p(\Delta\alpha\Delta T)/(bd_p)$ and $\Delta\sigma_{\text{CTE}} \approx M\alpha Gb\sqrt{\rho_{\text{th}}}$ with $M \approx 2.6\text{--}3.0$ and $\Delta T \approx 350 \pm 75$ K, contribute $\approx 24 \pm 6$ MPa. Load transfer is $\approx 1\text{--}2$ MPa at this V_p , while $\Delta\sigma_{\text{ss}} \approx 0$ because the matrix composition is unchanged. The sum ($\approx 51 \pm 8$ MPa) yields $YS_{\text{pred}} \approx 331 \pm 8$ MPa vs $YS_{\text{meas}} = 320$ MPa, consistent within uncertainty. The slight increase in ductility at 2 wt% arises from grain refinement and texture weakening, whereas >3 wt% promotes clustering that elevates local GND density and void nucleation, reducing work-hardening and ε_f . The hardening effect of nanoparticles arises from Orowan strengthening³⁶, load transfer and thermal mismatch strengthening. Microhardness measurements (Fig. 7b) show an almost linear increase with nanoparticle content; hardness rises from 81 HV for the unreinforced alloy to 102 HV for the 4 wt% composite³⁷. The increase matches the Hall-Petch relationship, reflecting grain refinement and particle strengthening³⁸. A statistical summary (mean \pm SD) of grain size, texture intensity (PF maxima and J-index), $\sigma_{0.2}$, UTS, ε_f , and HV for all conditions is provided in Table 1.

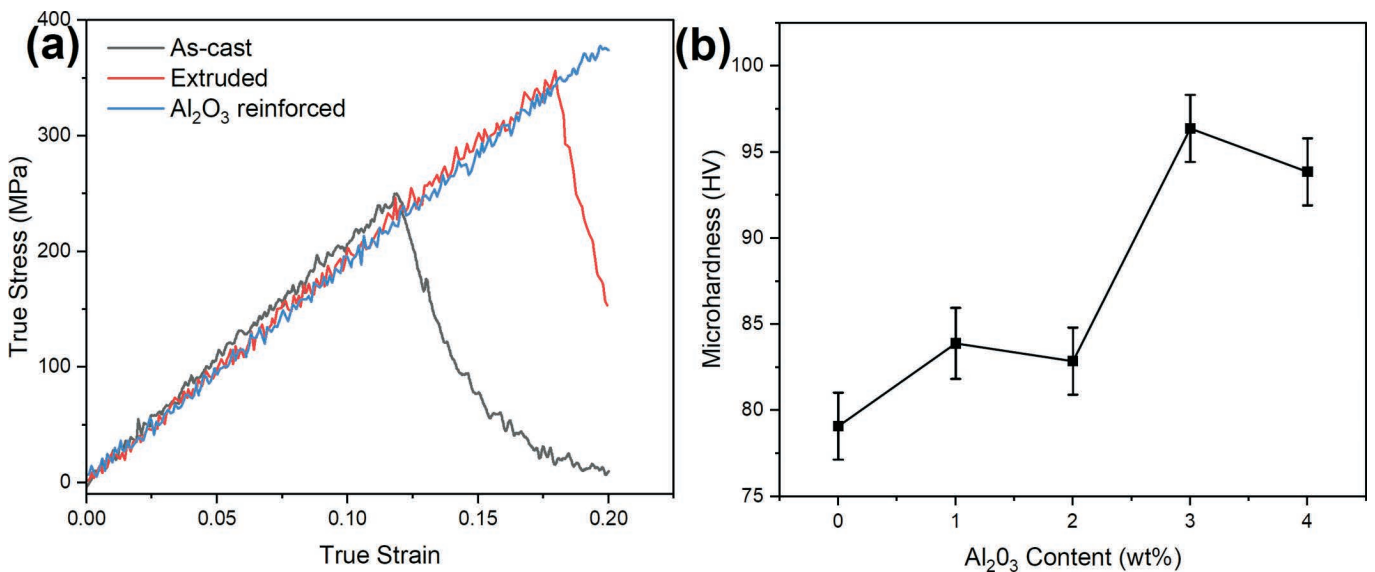


Fig. 7: (a) True stress-strain curves for the as-cast alloy, extruded alloy and Al₂O₃-reinforced composite at room temperature. (b) Microhardness as a function of Al₂O₃ nanoparticle content indicating a linear increase with reinforcement.

Table 1: Summary of mean \pm SD for microstructure, texture, and mechanical properties.

Condition	Grain size, μm (mean \pm SD)	(0002) PF max, MRD	J-index (-)	$\sigma_{0.2}$, MPa (mean \pm SD)	UTS, MPa (mean \pm SD)	ϵ_f , % (mean \pm SD)	HV (mean \pm SD)
As-cast	200 \pm 15	$\sim 8.5 \pm 0.4$	$\sim 8.2 \pm 0.3$	200 \pm 5	250 \pm 6	12.0 \pm 0.5	65 \pm 2
Extruded (unreinforced)	10.2 \pm 0.6	$\sim 6.1 \pm 0.3$	$\sim 6.0 \pm 0.3$	280 \pm 6	350 \pm 7	18.0 \pm 0.7	81 \pm 3
Extruded + 2 wt% Al_2O_3	6.1 \pm 0.4	$\sim 4.7 \pm 0.2$	$\sim 4.5 \pm 0.2$	320 \pm 7	380 \pm 8	20.0 \pm 0.6	102 \pm 4

(6) Dynamic recrystallization during hot deformation

The DRX behavior was analyzed in hot compression tests. Fig. 8a plots the recrystallized fraction as a function of true strain at 350–450 °C. DRX initiates at lower strains as temperature increases³⁹; at 450 °C, a significant fraction ($\sim 60\%$) of DRXed grains is achieved at a true strain of 0.2⁴⁰. The presence of Al_2O_3 nanoparticles accelerates DRX, shifting the sigmoidal curves to lower strains. This acceleration is attributed to particle-stimulated nucleation (PSN): large particles ($>1\ \mu\text{m}$) create high dislocation density zones that act as nuclei for new grains⁴¹. Although the nanoparticles are $\sim 35\ \text{nm}$, they tend to cluster locally; such clusters behave like micron-sized particles. Moreover, LPSO phases are known to stimulate DRX by providing nucleation sites⁴² and by acting as barriers to dislocation motion. The synergy between LPSO phases and Al_2O_3 clusters enhances recrystallization.

The EBSD map of a sample deformed to 50% strain at 400 °C (Fig. 8b) shows a necklace structure: fine equiaxed recrystallized grains surround elongated deformed grains⁴³. To substantiate texture weakening, we now include {0001} PFs and an ED-IPF and report PF maxima (m.r.d.) alongside texture indices (J-index and M-index) extracted from the EBSD-derived ODF; all confirm reduced basal texture after Al_2O_3 addition⁴⁴. In contrast,

the unreinforced alloy displays incomplete recrystallization with large unrecrystallized grains. Fig. 8c presents histograms of the Schmid factor distribution for F+E and Q+E samples, showing a higher average Schmid factor in the F+E sample due to a higher DRX fraction. The composite exhibits a similar distribution to the F+E sample, indicating that nanoparticles promote a high fraction of favorable orientations.

(7) Effect of Al_2O_3 content

Figure 9 plots the LPSO phase volume fraction versus processing temperature. LPSO fraction decreases from 0.35 at 300 °C to 0.12 at 500 °C because high temperatures dissolve plate-shaped LPSO precipitates into the Mg matrix⁴⁵. The presence of nanoparticles slightly increases the LPSO fraction at low temperatures due to restricted diffusion of RE elements. The microhardness plot and grain size histogram collectively show that increasing the nanoparticle content continuously refines the grains and enhances hardness⁴⁶. However, at high particle contents ($>3\ \text{wt}\%$) clusters become more frequent and the tensile elongation decreases slightly (not shown), indicating a trade-off between strengthening and ductility⁴⁷. The Schmid factor distribution and EBSD orientation map suggest that the composite retains a relatively weak texture, which contributes to improved formability.

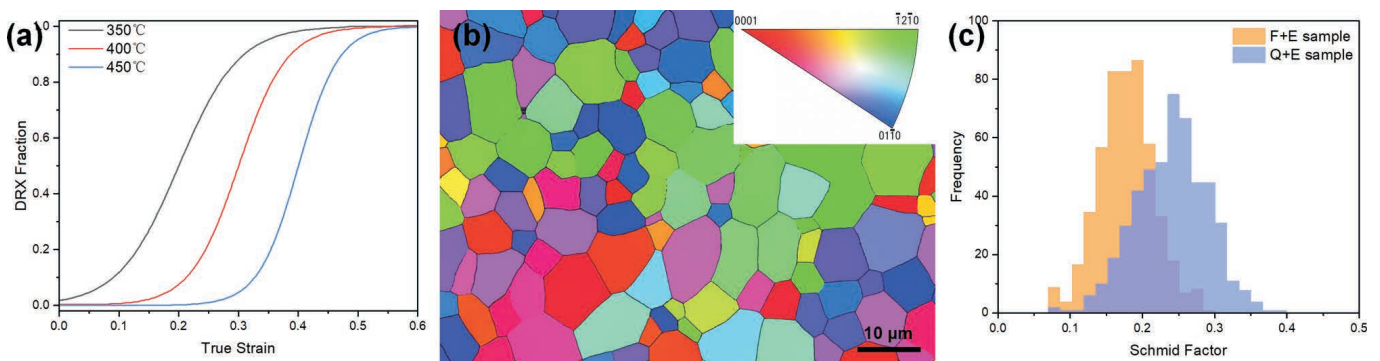


Fig. 8: (a) DRX fraction vs. true strain at 350–450 °C. (b) EBSD map with IPF color key and scale bar/magnification indicated. (c) Schmid factor histograms for F+E and Q+E.

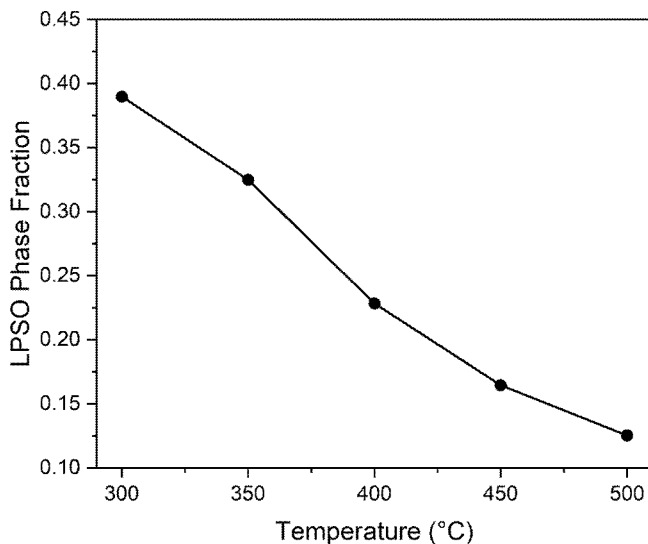


Fig. 9: LPSO phase volume fraction versus processing temperature; nanoparticles slightly increase the LPSO fraction at low temperatures.

IV. Conclusions

The incorporation of γ - Al_2O_3 nanoparticles into an Mg-Gd-Y alloy by means of stir-casting and extrusion significantly modifies the microstructure and improves mechanical performance. Characterization of the nanoparticles shows they measure ~ 35 nm in size, possess high purity and display characteristic FTIR and XRD signatures. Dispersion of these particles in the Mg matrix results in grain refinement from ~ 10 μm to ~ 6 μm and a reduction in texture intensity, attributed to heterogeneous nucleation during solidification and particle-stimulated recrystallization. XPS analysis reveals strong interfacial bonding with Al_2O_3 peaks at 74.8 eV and O 1s components characteristic of oxide and hydroxyl species. Mechanical testing demonstrates that the addition of 2 wt % Al_2O_3 nanoparticles increases the yield strength from 280 MPa to 320 MPa and the ultimate strength from 350 MPa to 380 MPa while preserving ductility. Microhardness increases linearly with nanoparticle content, consistent with grain refinement and Orowan strengthening. Hot compression tests combined with EBSD reveal that nanoparticles accelerate dynamic recrystallization; the recrystallized fraction reaches ~ 60 % at a true strain of 0.2 at 450 °C. Processing maps indicate an optimum hot working window near 400 °C and 0.01 – 0.1 s^{-1} strain rate. Fractography shows ductile dimpled fracture with strong particle-matrix bonding. Overall, the synergy between Al_2O_3 nanoparticles and LPSO phases enhances both room-temperature strength and high-temperature formability of the Mg-Gd-Y alloy. These findings suggest that nano-oxide reinforcement is an effective approach to optimize the mechanical properties of RE-containing Mg alloys while reducing the reliance on expensive alloying elements. Future work should explore the influence of nanoparticle size distribution and surface modifications on recrystallization kinetics and fatigue performance.

References

- Baral, S., Thawre, M., Sunil, B., Dumpala, R.: A review on developing high-performance ZE41 magnesium alloy by using bulk deformation and surface modification methods, *J. Magnes. Alloys*, **11**, 776–800, (2023). doi: <https://doi.org/10.1016/j.jma.2023.03.001>
- Geshani, M., Kalayeh, P., Asadi, A., Mirzadeh, H., Malekan, M., Emamy, M.: A review of mg alloys containing long-period stacking ordered (LPSO) structures with insight into the application of friction stir processing, *J. Mater. Res. Technol.*, **24**, 4945–4966, (2023). doi: <https://doi.org/10.1016/j.jmrt.2023.04.105>
- Basu, I., Chen, M., Wheeler, J., Schäublin, R., Löffler, J.: Stacking-fault mediated plasticity and strengthening in lean, rare-earth free magnesium alloys, *Acta Mater.*, **211**, 116877, (2021). doi: <https://doi.org/10.1016/j.actamat.2021.116877>
- Li, Z., Wang, J., Yan, R., Chen, Z., Ni, T., Dong, Z., Lu, T.: Effect of ce addition on hot deformation behavior and microstructure evolution of AZ80 magnesium alloy, *J. Mater. Res. Technol.*, **16**, 1339–1352, (2021). doi: <https://doi.org/10.1016/j.jmrt.2021.12.083>
- Zhang, X., Shi, Y., Li, J., Yue, H., Li, C., Ma, J., Jin, Q., Guo, S., Li, C., Chen, Q.: Effect of stacking faults and long period stacking order on mechanical properties for rare-earth magnesium alloy: As-cast versus as-solutioned, *J. Mater. Res. Technol.*, **29**, 1601–1615, (2024). doi: <https://doi.org/10.1016/j.jmrt.2024.01.214>
- Xu, C., Nakata, T., Qiao, X., Zheng, M., Wu, K., Kamado, S.: Effect of LPSO and SFs on microstructure evolution and mechanical properties of mg-gd-Y-Zn-zr alloy, *Sci. Rep.*, **7**, 40846, (2017). doi: <https://doi.org/10.1038/srep40846>
- Garcés, G., Medina, J., Pérez, P., Barea, R., Lim, H., Kim, S., Maawad, E., Schell, N., Adeva, P.: Study of tensile and compressive behavior of ECO-Mg₉₇Gd₂Zn₁ alloys containing long-period stacking ordered phase with lamellar structure, *Metals*, **14**, 530, (2024). doi: <https://doi.org/10.3390/met14050530>
- Mahinroosta, M., Allahverdi, A.: Production of nanostructured γ -alumina from aluminum foundry tailing for catalytic applications, *Int. Nano Lett.*, **8**, 255–261, (2018). doi: <https://doi.org/10.1007/s40089-018-0247-1>
- Krishna, D., Philip, J.: Review on surface-characterization applications of X-ray photoelectron spectroscopy (XPS): recent developments and challenges, *Appl. Surf. Sci. Adv.*, **12**, 100332, (2022). doi: <https://doi.org/10.1016/j.apsadv.2022.100332>
- Zhang, Z., Wang, L., Zeng, M., Zeng, R., Lin, C., Wang, Z., Chen, D., Zhang, Q.: Corrosion resistance and superhydrophobicity of one-step polypropylene coating on anodized AZ31 mg alloy, *J. Magnes. Alloys*, **9**, 1443–1457, (2020). doi: <https://doi.org/10.1016/j.jma.2020.06.011>
- Syrkov, A., Ngo, K., Taraban, V., Tomaev, B.: Formation of hydrophobic surface compounds of metals by solid-state synthesis using silicon hydride reagents, *Bull. St. Petersburg State Inst. Technol.*, **68**, 33–39, (2024). doi: <https://doi.org/10.36807/1998-9849-2024-68-94-33-39>
- Łozinko, A., Gholizadeh, R., Zhang, Y., Klement, U., Tsuji, N., Mishin, O., Guo, S.: Evolution of microstructure and mechanical properties during annealing of heavily rolled AlCoCrFeNi_{2.1} eutectic high-entropy alloy, *Mater. Sci. Eng. A*, **833**, 142558, (2021). doi: <https://doi.org/10.1016/j.msea.2021.142558>
- Karthik, R., Sankaran, N., Raja, K., Venkatesh, R.: Characteristics performance evaluation of AZ91-fly ash composite developed by vacuum associated stir processing, *Int. J. Cast Met. Res.*, 1–8, (2024). doi: <https://doi.org/10.1080/13640461.2024.2364129>

- 14 Larraza, A., Burke, S., Bagha, P., Razavi, M.: Fabrication and processing of magnesium-based metal matrix nanocomposites for bioabsorbable implants, *Metals*, **14**, 1318, (2024). doi: <https://doi.org/10.3390/met14121318>
- 15 Chen, B., Qi, L., Fu, J., Zhang, Q., Zhou, J.: Preparation of the high compressive performance special-shaped Csf/AZ91D composite part using the liquid-solid extrusion following vacuum pressure infiltration process, *J. Magnes. Alloys*, **13**, 1617–1629, (2024). doi: <https://doi.org/10.1016/j.jma.2024.04.034>
- 16 Wu, Z., Zhang, C., Zhu, Y., Lu, Z., Liu, H., Xu, B., Zhang, X., Tian, W.: Visualization of macrophase separation and transformation in immiscible polymer blends, *CCS Chem.*, **5**, 718–728, (2022). doi: <https://doi.org/10.31635/ccschem.022.202101726>
- 17 Helal, M., Fadl-Alah, A., Baraka, Y., Gad, M., Emam, A.: In-vitro comparative evaluation for the surface properties and impact strength of CAD/CAM milled, 3D printed, and polyamide denture base resins, *J. Int. Soc. Prev. Community Dent.*, **12**, 126–131, (2022). https://doi.org/10.4103/jispcd.jispcd_293_21
- 18 Zhong, J., Xu, Q.: High-temperature mechanical behaviors of SiO₂-based ceramic core for directional solidification of turbine blades, *Materials*, **13**, 4579, (2020). doi: <https://doi.org/10.3390/ma13204579>
- 19 Li, X., Hou, L., Wei, Y., Wei, Z.: Constitutive equation and hot processing map of a nitrogen-bearing martensitic stainless steel, *Metals*, **10**, 1502, (2020). doi: <https://doi.org/10.3390/met10111502>
- 20 Egzar, H., Yahya, W., Ridha, N., Sahap, E.: Electrochemical preparation of aluminum oxide nanoparticles and using for remove chromotrope-E122 dye, *Int. J. Health Sci.*, 7613–7620, (2022). doi: <https://doi.org/10.53730/ijhs.v6ns3.7764>
- 21 Wang, T., Yin, Z., Guo, Y., Bai, F., Chen, J., Dong, W., Liu, J., Hu, Z., Chen, L., Li, Y., Su, B.: Highly selective photocatalytic conversion of glucose on holo-symmetrically spherical three-dimensionally ordered macroporous heterojunction photonic crystal, *CCS Chem.*, **5**, 1773–1788, (2022). doi: <https://doi.org/10.31635/ccschem.022.202202213>
- 22 Yang, H., Wang, X., Zheng, T., Cantillo, N., Goenaga, G., Zawadzinski, T., Tian, H., Wright, J., Meulenberg, R., Wang, X., Xia, Z., Ma, S.: CrN-encapsulated hollow Cr-N-C capsules boosting oxygen reduction catalysis in PEMFC, *CCS Chem.*, **3**, 208–218, (2020). doi: <https://doi.org/10.31635/ccschem.020.202000645>
- 23 Baldovino-Medrano, V., Niño-Celis, V., Giraldo, R.: Systematic analysis of the nitrogen Adsorption-Desorption isotherms recorded for a series of materials based on Microporous-Mesoporous amorphous aluminosilicates using classical methods, *J. Chem. Eng. Data*, **68**, 2512–2528, (2023). doi: <https://doi.org/10.1021/acs.jced.3c00257>
- 24 Naiel, B., Fawzy, M., Halmy, M., Mahmoud, A.: Green synthesis of zinc oxide nanoparticles using sea lavender (*Limonium pruinosa* L. Chaz.) extract: characterization, evaluation of anti-skin cancer, antimicrobial and antioxidant potentials, *Sci. Rep.*, **12**, 20370, (2022). doi: <https://doi.org/10.1038/s41598-022-24805-2>
- 25 El-Belely, E., Farag, M., Said, H., Amin, A., Azab, E., Gobouri, A., Fouda, A.: Green synthesis of zinc oxide nanoparticles (ZnO-NPs) using *arthrospira platensis* (Class: Cyanophyceae) and evaluation of their biomedical activities, *Nanomaterials*, **11**, 95, (2021). doi: <https://doi.org/10.3390/nano11010095>
- 26 Injor, O., Daramola, O., Adewuyi, B., Adediran, A., Ramakokovhu, M., Sadiku, R., Akinlabi, E.: Grain refinement of Al-Zn-Mg alloy during equal channel angular pressing (ECAP), *Results Eng.*, **16**, 100739, (2022). doi: <https://doi.org/10.1016/j.rineng.2022.100739>
- 27 Wei, Z., Mu, W., Liu, S., Wang, F., Zhou, L., Wang, Z., Mao, P., Liu, Z.: Effects of gd on hot tearing susceptibility of as-cast Mg_{96.94}-Zn₁-Y_(2-x)-Gd_x-Zr_{0.06} alloys reinforced with lps phase, *J. Alloys Compd.*, **926**, 166895, (2022). doi: <https://doi.org/10.2139/ssrn.4143230>
- 28 Jiang, M., Xu, C., Yan, H., Nakata, T., Chen, Z., Lao, C., Chen, R., Kamado, S., Han, E.: Quasi-in-situ observing the rare earth texture evolution in an extruded mg-zn-gd alloy with bimodal microstructure, *J. Magnes. Alloys*, **9**, 1797–1805, (2020). doi: <https://doi.org/10.1016/j.jma.2020.09.001>
- 29 Chaudhary, V., Verma, R., Sharma, V.: Effect of nanoparticles adhesion and multipass friction stir processing on metallurgical properties of AZ91D magnesium alloy, *J. Adhes. Sci. Technol.*, **38**, 1953–1973, (2023). doi: <https://doi.org/10.1080/01694243.2023.2282828>
- 30 Zheng, X., Xue, Y., Zhang, C., Li, Y.: Controlled growth of multidimensional interface for high-selectivity ammonia production, *CCS Chem.*, **5**, 1653–1662, (2022). doi: <https://doi.org/10.31635/ccschem.022.202202189>
- 31 Fan, H., Li, X., Zhou, J., Wang, X., Gao, X., Hu, H., Zhou, L., Cai, T., Cui, Y., Liu, P., Xue, Q., Yan, Z., Xing, W.: Realizing the long lifespan of molybdenum trioxide in aqueous aluminum ion batteries through potential regulation, *Renewables*, **1**, 455–464, (2023). doi: <https://doi.org/10.31635/renewables.023.202200019>
- 32 Zhong, S., Wang, Y., Lan, J., Xie, M., Wu, Y., Li, J., Liu, F., Jiang, L., Peng, J., Yuan, L., Zhai, M., Shi, W.: Radiation-assisted synthesis of crown ether-modified covalent organic frameworks for lithium isotope separation, *CCS Chem.*, **6**, 2594–2606, (2024). doi: <https://doi.org/10.31635/ccschem.024.202303787>
- 33 Luo, T., Wang, Z., Han, X., Chen, Y., Iuga, D., Lee, D., An, B., Xu, S., Kang, X., Tuna, F., McInnes, E., Hughes, L., Spencer, B., Schröder, M., Yang, S.: Efficient photocatalytic reduction of CO₂ catalyzed by the Metal-Organic framework MFM-300(Ga), *CCS Chem.*, **4**, 2560–2569, (2022). doi: <https://doi.org/10.31635/ccschem.022.202201931>
- 34 Lin, R., Liu, B., Zhang, J., Zhang, S.: Microstructure evolution and properties of 7075 aluminum alloy recycled from scrap aircraft aluminum alloys, *J. Mater. Res. Technol.*, **19**, 354–367, (2022). doi: <https://doi.org/10.1016/j.jmrt.2022.05.011>
- 35 Wu, Y., Wang, H., Ban, C.: Effect of fe content on the microstructure and properties of Hot-extruded 6061 aluminum alloy, *J. Phys. Conf. Ser.*, **1986**, 012011, (2021). doi: <https://doi.org/10.1088/1742-6596/1986/1/012011>
- 36 Subramani, M., Huang, S., Borodianskiy, K.: Effect of SiC nanoparticles on AZ31 magnesium alloy, *Materials*, **15**, 1004, (2022). doi: <https://doi.org/10.3390/ma15031004>
- 37 Mercado-Lemus, V., Gómez-Esparza, C., Díaz-Guillén, J., Mayén, J., Flores-Gallegos, A., Arcos-Gutiérrez, H., Hernández-Hernández, M., Garduño, I., Betancourt-Cantera, J., Pérez-Bustamante, R.: Wear dry behavior of the Al-6061-Al₂O₃ composite synthesized by mechanical alloying, *Metals*, **11**, 1652, (2021). doi: <https://doi.org/10.3390/met11101652>
- 38 Dangwal, S., Edalati, K., Valiev, P., Langdon, T.: Breaks in the Hall-Petch relationship after severe plastic deformation of magnesium, aluminum, copper, and iron, *Crystals*, **13**, 413, (2023). doi: <https://doi.org/10.3390/cryst13030413>
- 39 Jaimin, A., Kotkunde, N., Singh, S., Saxena, K.: Studies on flow stress behaviour prediction of AZ31B alloy: microstructural evolution and fracture mechanism, *J. Mater. Res. Technol.*, **27**, 5541–5558, (2023). doi: <https://doi.org/10.1016/j.jmrt.2023.10.206>

- 40 Tian, Y., Zhang, P., Zhao, G., Li, H., Ma, L., Li, J.: A systematic study on thermo-mechanical behavior, processing maps and recrystallization mechanism of Incoloy825 superalloy during hot compression, *J. Mater. Res. Technol.*, **28**, 4551–4566, (2024). doi: <https://doi.org/10.1016/j.jmrt.2024.01.042>
- 41 Mirzadeh, H.: Grain refinement of magnesium alloys by dynamic recrystallization (DRX): A review, *J. Mater. Res. Technol.*, **25**, 7050–7077, (2023). doi: <https://doi.org/10.1016/j.jmrt.2023.07.150>
- 42 Zhang, N., Liu, M., Li, Q., Chen, X., Zheng, Z.: Effect of long-period stacking ordered phase on dynamic recrystallization in Mg-Y-Zn-zr alloy processed by backward extrusion, *J. Mater. Res. Technol.*, **26**, 2384–2393, (2023). doi: <https://doi.org/10.1016/j.jmrt.2023.08.089>
- 43 Moretti, M., Dalai, B., Åkerström, P., Arvieu, C., Jacquin, D., Lacoste, É., Lindgren, L.: High strain rate deformation behavior and recrystallization of alloy 718, *Metall. Mater. Trans. A*, **52**, 5243–5257, (2021). doi: <https://doi.org/10.1007/s11661-021-06463-7>
- 44 Yan, Z., Li, L., Zhu, J., Ren, L., Xue, Y., Wang, Q., Zhang, Z.: Deformation behavior of LPSO phases, grain refinement mechanism, and texture evolution of a mg-gd-Y-Zn-zr alloy processed by forward extrusion combined with dual-directional angular deformation, *J. Mater. Res. Technol.*, **28**, 4131–4141, (2024). doi: <https://doi.org/10.1016/j.jmrt.2024.01.032>
- 45 Yin, J., Liu, Y., Zhu, G.: Microstructural evolution and thermal stability of long period stacking ordered phases in Mg₉₇Er₂Ni₁ and Mg₉₇Er₂Zn₁ alloys, *Crystals*, **14**, 1092, (2024). doi: <https://doi.org/10.3390/cryst14121092>
- 46 Tan, Z., Li, J., Zhang, Z.: Experimental and numerical studies on fabrication of nanoparticle reinforced aluminum matrix composites by friction stir additive manufacturing, *J. Mater. Res. Technol.*, **12**, 1898–1912, (2021). doi: <https://doi.org/10.1016/j.jmrt.2021.04.004>
- 47 Song, X., Bayati, P., Gupta, M., Elahinia, M., Haghshenas, M.: Fracture of magnesium matrix nanocomposites - A review, *Int. J. Lightweight Mater. Manuf.*, **4**, 67–98, (2020). doi: <https://doi.org/10.1016/j.ijlmm.2020.07.002>